SCIENTIFIC REPORTS

OPEN

MoS_2 Heterojunctions by Thickness Modulation

Mahmut Tosun[1,2,3,*], Deyi Fu[2,4,*], Sujay B. Desai[1,2,3,*], Changhyun Ko[4], Jeong Seuk Kang[1,2,3], Der-Hsien Lien[1,2,3], Mohammad Najmzadeh[1,3], Sefaattin Tongay[4], Junqiao Wu[2,4] & Ali Javey[1,2,3]

Received: 03 February 2015
Accepted: 05 May 2015
Published: 30 June 2015

In this work, we report lateral heterojunction formation in as-exfoliated MoS_2 flakes by thickness modulation. Kelvin probe force microscopy is used to map the surface potential at the monolayer-multilayer heterojunction, and consequently the conduction band offset is extracted. Scanning photocurrent microscopy is performed to investigate the spatial photocurrent response along the length of the device including the source and the drain contacts as well as the monolayer-multilayer junction. The peak photocurrent is measured at the monolayer-multilayer interface, which is attributed to the formation of a type-I heterojunction. The work presents experimental and theoretical understanding of the band alignment and photoresponse of thickness modulated MoS_2 junctions with important implications for exploring novel optoelectronic devices.

Semiconducting transition metal dichalcogenides (TMDCs) with a layered crystal structure exhibit unique electrical[1,2] and optical properties[3–5]. TMDCs provide opportunities in exploring new device concepts given their atomic level flatness, and ability to form van der Waals (vdW) heterostructures with strong interlayer coupling[6–8]. For instance, vdW heterobilayers of MoS_2/WSe_2 have been recently reported to exhibit spatially *direct* light absorption but spatially *indirect* light emission, representing a highly intriguing material property[9,10]. Here, we explore the optoelectronic properties of lateral "hetero"-junctions formed on a single crystal of MoS_2 of varying thickness (i.e., number of layers). As a result of the quantum confinement effect[11], when the thickness of a MoS_2 crystal is scaled down to a monolayer the optical band gap increases from 1.29 eV (indirect) to 1.85 eV (direct)[12,13]. The change in the band structure and the electron affinity of MoS_2 with layer number opens up the path to the formation of atomically sharp heterostructures, not by changing composition but rather by changing layer thickness[14]. We experimentally examine the surface potential of this thickness modulated heterojunction by using Kelvin probe force microscopy (KPFM). We further use scanning photocurrent microscopy (SPCM) to probe the photoresponse of the junction. A large photocurrent response is observed at the monolayer/multilayer junction interface which confirms the presence of a strong built-in electric field at the interface. Device modeling is used in parallel to experiments to understand the underlying mechanism of the observed photocurrents and the band-alignments at the junction interface, suggesting the formation of a type-I heterojunction.

SPCM has been previously used to study the photoresponse of metal contacted MoS_2 transistors, where the channel thickness for MoS_2 was uniform throughout the device[15,16]. The results have shown that the photoresponse is primarily driven by the metal/MoS_2 Schottky contacts and photothermoelectric effect[16]. In distinct contrast to previous studies, we observe that the peak photoresponse is spatially located at the MoS_2 monolayer/multilayer junction for our lateral heterojunctions and not at the metal contacts.

[1]Electrical Engineering and Computer Sciences, University of California, Berkeley, CA, 94720. [2]Materials Sciences Division, Lawrence Berkeley National Laboratory, Berkeley, CA 94720. [3]Berkeley Sensor and Actuator Center, University of California, Berkeley, CA, 94720. [4]Department of Materials Science and Engineering, University of California, Berkeley, CA, 94720. *These authors contributed equally to this work. Correspondence and requests for materials should be addressed to A.J. (email: ajavey@eecs.berkeley.edu)

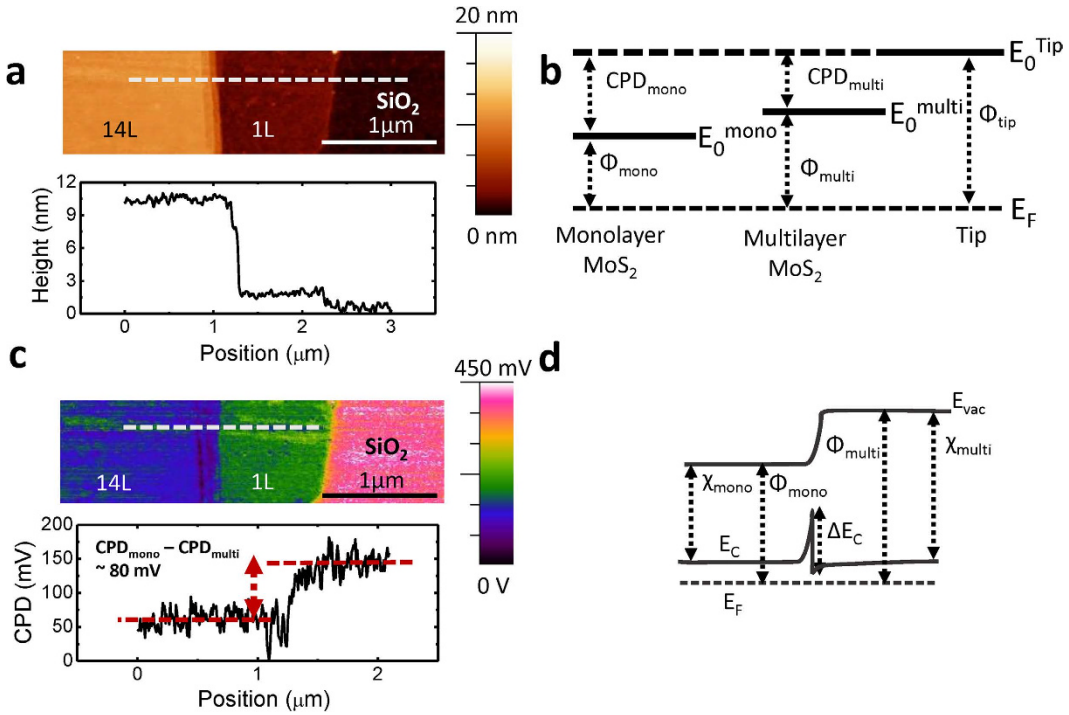

Figure 1. **a**. Atomic Force Microscope (AFM) image of a monolayer-multilayer MoS_2 flake. **b.** Representative energy band diagrams of isolated monolayer and multilayer MoS_2 with respect to the AFM tip, depicting CPD and work function values. **c.** Kelvin Force Probe Microscope (KPFM) image of a representative 1L-14L MoS_2 flake. **d.** Representative band diagram of a monolayer-multilayer device at equilibrium.

Results

Band offset extraction at the monolayer-multilayer MoS_2 junction. KPFM is performed to spatially map the surface potential, and shed light on the band offsets at the monolayer-multilayer interface. The sample surface topography and contact potential difference (CPD) between the tip and sample are measured simultaneously[17,18]. Figure 1a demonstrates a monolayer-multilayer junction flake with 10 nm of multilayer (~14 layers; 14 L) thickness. In this particular flake, monolayer to multilayer transition occurs across ~100 nm of the lateral distance in a terraced manner. KPFM is performed using a Bruker MultiMode atomic force microscope under ambient conditions. A Si cantilever tip coated with Pt-Ir (SCM-PIT, Bruker Co.) is used in the tapping mode. Electrical contacts to the MoS_2 flake were grounded during the measurements. An AC voltage of 2 V is applied to the tip while the tip height is kept constant at 5 nm. The measured DC voltage of the tip, corresponding to CPD, determines the work function difference between the AFM tip (Pt-Ir) and each region of the MoS_2 flake[19,20], i.e., $\mathrm{CPD_{mono}} = \frac{(\Phi_{tip} - \Phi_{mono})}{e}$ for the monolayer side and $\mathrm{CPD_{multilayer}} = \frac{(\Phi_{tip} - \Phi_{multilayer})}{e}$ for the multilayer side. Φ_{mono}, $\Phi_{multilayer}$, and Φ_{tip} are the work functions of monolayer MoS_2, multilayer MoS_2 and the surface of AFM tip, respectively (Fig. 1b). The measured surface potential difference, $\Delta\mathrm{CPD} = \mathrm{CPD_{mono}} - \mathrm{CPD_{multilayer}} = \left(\frac{\Phi_{multilayer} - \Phi_{monolayer}}{e}\right)$, corresponds to the band bending in the vacuum level E_{vac} at thermal equilibrium, and is also equal to the workfunction difference between the monolayer and the multilayer (Fig. 1b). KPFM map of a representative 1 L–14 L flake is shown in Fig. 1c. From KPFM measurements, the workfunction difference is found to be ~80 meV (Fig. 1c)[21,22]. Next, we focus on obtaining the energy band diagram for the heterojunction by first extracting the conduction band offset at the interface. The conduction band offset $\Delta E_C = (\chi_{multilayer} - \chi_{mono})$ at the heterojunction corresponds to the electron affinity difference between the monolayer (χ_{mono}) and multilayer ($\chi_{multilayer}$). The workfunction difference between monolayer and multilayer is related to effective density of states (N_C), ΔE_C and doping levels (N_D) as shown in Eq. 1. Here, k is the Boltzmann constant and T is the temperature.

$$\Phi_{multi-mono} = \left[\Delta E_C - kT\left(\ln\frac{\left(\frac{N_{D,multi}}{N_{C,multi}}\right)}{\left(\frac{N_{,Dmono}}{N_{C,mono}}\right)}\right)\right] \quad (1)$$

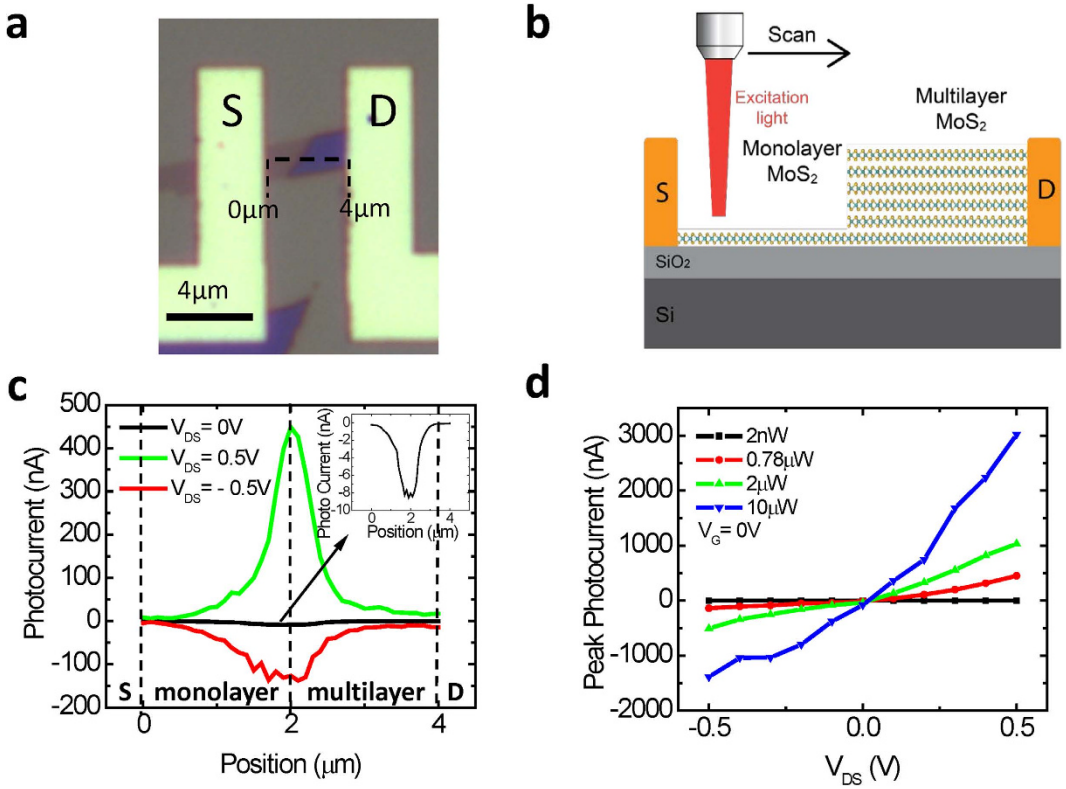

Figure 2. a. Optical microscope image of the monolayer-multilayer device with Ni/Au (30 nm/30 nm) contacts. **b.** Schematic representation of the SPCM measurement. **c.** Photoresponse of the monolayer-multilayer MoS_2 flake versus position along the dashed line at $V_G = 0$ V, with illumination power of 0.78 μW and with $V_{DS} = -0.5$ V, $V_{DS} = 0.5$ V and $V_{DS} = 0$ V. **d.** Peak photocurrent vs. V_{DS} at $V_{GS} = 0$ V with different illumination powers.

Boltzmann approximation is considered while deriving Eq. 1. Next we assume the doping level per unit volume is identical in both monolayer and multilayer flakes. Thus Eq. 1 becomes,

$$\Phi_{\text{multi-mono}} = \Delta E_C - kT\left(\frac{3}{2}\right)\ln\left(\frac{(m_n^*)_{\text{mono}}}{(m_n^*)_{\text{multi}}}\right) \quad (2)$$

$\Phi_{\text{multi-mono}}$ is measured from KPFM, effective mass values for electrons are taken to be $m^*_{n,\text{mono}} = 0.407\ m_0$ and $m^*_{n,\text{multi}} = 0.574\ m_0$. From these parameters, ΔE_C of ~70 meV at the 1 L–14 L interface is extracted. This band offset corresponds to a type-I heterojunction as depicted in the qualitative band diagram of Fig. 1d. Note that the relative values of the dielectric constant of monolayer and multilayer MoS_2 determine the electric fields and hence the band bending on both sides of the heterojunction. The dielectric constants are assumed to be the same (~4) in this work[24].

Photoresponse at the monolayer-multilayer MoS_2 junction. Scanning photocurrent microscopy (SPCM), a spatially resolved photodetection technique that combines electrical measurement and local illumination with a focused laser beam is used to probe the local photoresponse of the monolayer-multilayer MoS_2 devices[25–30]. Optical image of a representative device is shown in Fig. 2a. Here, the device consists of a 1 L–5 L MoS_2 junction. The channel lengths for the monolayer and the multilayer regions are ~2 μm each. The contact to the monolayer is defined as the source electrode and is electrically grounded. The contact to the multilayer MoS_2 serves as the drain electrode to which an external voltage, V_{DS} is applied during the measurements. The heavily doped Si substrate serves as the global back-gate to which voltage, V_G can be applied to modulate the electric potential in MoS_2. The device is locally illuminated by a focused laser beam (wavelength: 488 nm, diameter: ~1 μm) as depicted in Fig. 2b. The spatial resolution of the scanning stage is 0.1 μm. The light current, I_{light} is recorded as the laser spot is scanned across the length of the device. The photocurrent, $I_{\text{photocurrent}}$, is then obtained as a function of illumination spot by subtracting the dark current of the device, I_{dark}, from I_{light}. In contrast to previous reports studying the photoresponse in MoS_2 single layer or multilayer devices (Fig. S2)[3,15,16,31], the peak photocurrent in our device is observed at the monolayer-multilayer interface rather than the metal/semiconductor junction. Figure 2c shows the spatial response of the photocurrent along the dashed line

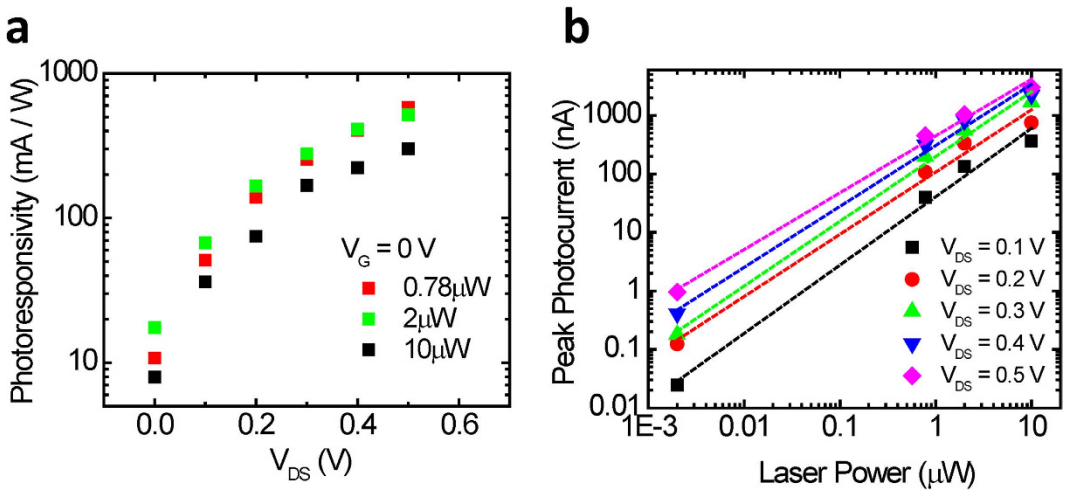

Figure 3. a. Photoresponsivity vs. the applied V_{DS} at $V_G = 0$ V and with different laser power. **b.** Peak photocurrent vs. laser power at $V_G = 0$ V and at different V_{DS} values.

of Fig. 2a at $V_G = 0$ V and laser intensity of 0.78 μW. Source-drain voltage is varied from −0.5 V to 0.5 V. Even without source drain bias ($V_{DS} = 0$ V), a finite short circuit current (~8 nA) is measured as seen in the inset of Fig. 2c. This implies that the expected band bending and the resulting built-in electric field that is induced by the difference in the electron affinities of the monolayer and multilayer MoS_2 regions is capable of separating the electron-hole pairs generated at the monolayer-multilayer interface. The dependence of the photocurrent on V_{DS} and the excitation power is investigated to further characterize the monolayer-multilayer junction devices. The peak photocurrent, corresponding to the local illumination of the monolayer-multilayer interface, is measured at different illumination intensities of 2 nW, 0.78 μW, 2 μW and 10 μW and V_{DS} of −0.5 V to 0.5 V at $V_{GS} = 0$ V (Fig. 2d). The photocurrent increases as the applied V_{DS} bias is increased due to the contribution of the enhanced drift current and decreased transit time of the electrons[3]. The increase in the photocurrent with the illumination can be attributed to generation of higher number of electron-hole pairs. It is important to note that at all different laser powers and V_{DS} values the peak photocurrent response is observed at the monolayer-multilayer heterojunction.

Photoresponsivity at the monolayer-multilayer MoS_2 junction. To further characterize the photocurrent generation at the heterojunction, photoresponsivity is experimentally investigated as a function of V_{DS} and laser power. Photoresponsivity determines the gain of a photodetector system in terms of the ratio of photocurrent generated ($I_{photocurrent}$) and the incident laser power ($P_{incident}$), i.e., ($I_{photocurrent}$) / $P_{incident}$. Figure 3a shows the photoresponsivity with varying laser powers at $V_G = 0$ V. It is found to increase as the V_{DS} increases from 0 V to 0.5 V. The maximum photoresponsivity is found to be 580 mA / W at $V_{DS} = 0.5$ V and with the power of 0.78 μW. Given the power of the laser (0.78 μW) and the V_{DS} value of 0.5 V and at $V_G = 0$ V, the maximum photoresponsivity of the monolayer – multilayer heterojunction is found to be greater than the highest reported MoS_2 photodetector in the literature[3,15,31,32]. Moreover, the dependence of the photocurrent on power is investigated. Figure 3b shows a linear relationship between the peak photocurrent and the laser power. This is consistent with the response of standard photodiodes where the photocurrent is proportional to the carrier generation rate and hence the light intensity[33].

Dependence of the peak photocurrent on the gate bias. Next, we explore the effect of gate voltage on the peak photocurrent. Figure 4a shows the measured photocurrent as a function of displacement along the length of the device for V_{GS} ranging from −30 V to 30 V. The drain voltage is maintained constant at 1 V with an illumination power of 2 μW. The effect of gate voltage on the photocurrent is minimal. This is further illustrated in Fig. 4b where the peak photocurrent is plotted as a function of gate voltage. For comparison the dark current as a function of gate voltage for the same device is also shown. While the dark current shows strong gate dependency, consistent with n-type characteristics of MoS_2, the light current exhibits nearly no gate dependence. This is distinct from the previous studies of photocurrent for a uniform thickness MoS_2 flake, where the gate voltage was shown to modulate the Schottky barrier heights and thus the photoresponse[34]. In contrast, the peak photocurrent in our devices arise from the monolayer-multilayer junction where the global back-gate has minimal effect on its potential profile.

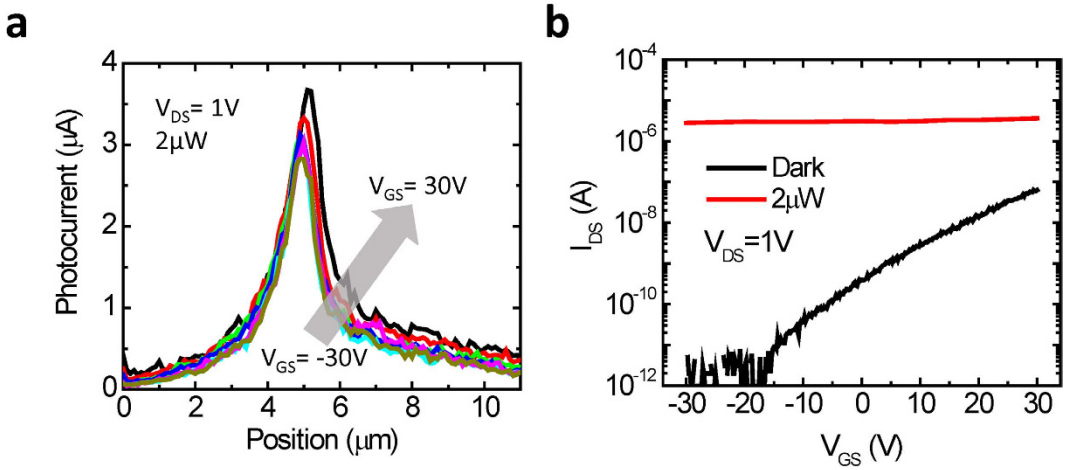

Figure 4. **a**. Photocurrent vs. position at $V_{DS} = 1$ V with illumination power of 2 μW and V_{GS} varied from −30 V to 30 V at 10 V increments. **b.** I_{DS} vs. V_{GS} at $V_{DS} = 1$ V in dark and with 2 μW of illumination power.

Discussion

Device modeling was performed using TCAD Sentaurus to further understand the junction properties for a monolayer-multilayer device. For the Sentaurus simulations a $\Delta E_C \sim 70$ meV, calculated from the KPFM data is used. The doping level for both monolayer and multilayer regions are assumed to be $N_{D,mono} = N_{D,multi} = 10^{18}$ cm^{-3}[35]. The effect of the back gate is modeled as a change in the device doping concentration. The effective mass values are taken to be $m^*_e \sim 0.407$ m_0 for the monolayer and $m^*_e \sim 0.574$ m_0 for the multilayer as described earlier[23]. The dielectric constants are assumed to be the same $\varepsilon_{mono} = \varepsilon_{multilayer} = 4\,\varepsilon_0$[24]. For the simulated device, the exact dimensions of the measured device presented in Fig. 2 are used. Electron affinities are assumed to be $\chi_{monolayer} = 4$ eV[36] and $\chi_{multilayer} = 4.07$ eV, such that $\Delta E_C = 70$ meV as obtained earlier using the experimental KPFM data. Measured values for bandgap of monolayer (1.85 eV) and 5 layers (1.4 eV) are used[12]. A light window of 1 μm is used that corresponds to the spot size of the laser and is shined in the center of the junction. A laser wavelength of 488 nm and an absorption coefficient of 10^6 cm^{-1} for the monolayer and 10^5 cm^{-1} for the multilayer side is assumed for the simulations[15,37]. Thus with the assumptions stated above and using the KPFM information, simulations revealed a type – I heterojunction band alignment in the monolayer – multilayer MoS_2 heterojunction flake as seen in Fig. 5a–c.

Figure 5a shows the simulated band diagram at $V_{DS} = 0$ V for the dark condition and when light is illuminated at the monolayer-multilayer interface. Under illumination, Fermi levels split ($E_{F,n}$ and $E_{F,p}$) as a result of the generation of the electron hole pairs. At a simulated laser power of 0.78 μW, low level injection conditions prevail and no change in the quasi Fermi level for electrons is observed as seen in Fig. 5a. At zero V_{DS} bias, due to the built-in electric field at the heterojunction, electrons that are generated at the monolayer side of the monolayer-multilayer junction are swept to the monolayer side (source). However electrons generated at the multilayer side are subjected to a barrier height of 70 meV. Holes do not encounter any barrier and freely move to the multilayer side (drain). This is consistent with the measured SPCM data, where a negative photocurrent of 8 nA is recorded at zero V_{DS} signifying that the electrons are collected at the source (monolayer) and holes at the drain (multilayer) side.

Previous studies have shown small Schottky barrier heights for electrons both in monolayer and multilayer MoS_2, on the order of 200 meV or less[38–41]. The barrier height for electrons at the monolayer-multilayer interface is $\Delta E_C = 70$ meV as calculated. In this system, the Schottky barrier height at the contacts and the barrier height at the junction are on the same order of magnitude. Therefore a part of the applied VDS gets dropped at the contacts, and the remaining voltage is dropped at the monolayer-multilayer MoS_2 interface. When a negative V_{DS} (Fig. 5b) is applied to the multilayer side (drain), there is a higher built-in electric field and a wider depletion region at the junction. A wider depletion region at the monolayer side allows the separation of a larger number of photogenerated electron-hole pairs thus resulting in a larger negative photocurrent compared to the case of zero V_{DS} as the electrons get swept to the monolayer side (source) and holes swept to the multilayer side (drain) freely. However electrons generated at the multilayer side still face a barrier height of ~70 meV, just like in the case of zero bias. By applying a positive V_{DS} (Fig. 5c) the barrier height for electron transport from the monolayer to the multilayer is nearly diminished. Electron-hole pairs generated at the monolayer side contribute to the photocurrent since holes move to the monolayer side (source) freely and electrons can go over the decreased barrier height and move to the multilayer side (drain). Whereas, electron-hole pairs generated at the multilayer side don't contribute to the photocurrent since holes see a barrier of ΔE_V (~0.38 eV). This current flow mechanism is consistent with measuring positive photocurrent at $V_{DS} > 0$ and measuring negative photocurrent for $V_{DS} < 0$ as seen in Fig. 2d.

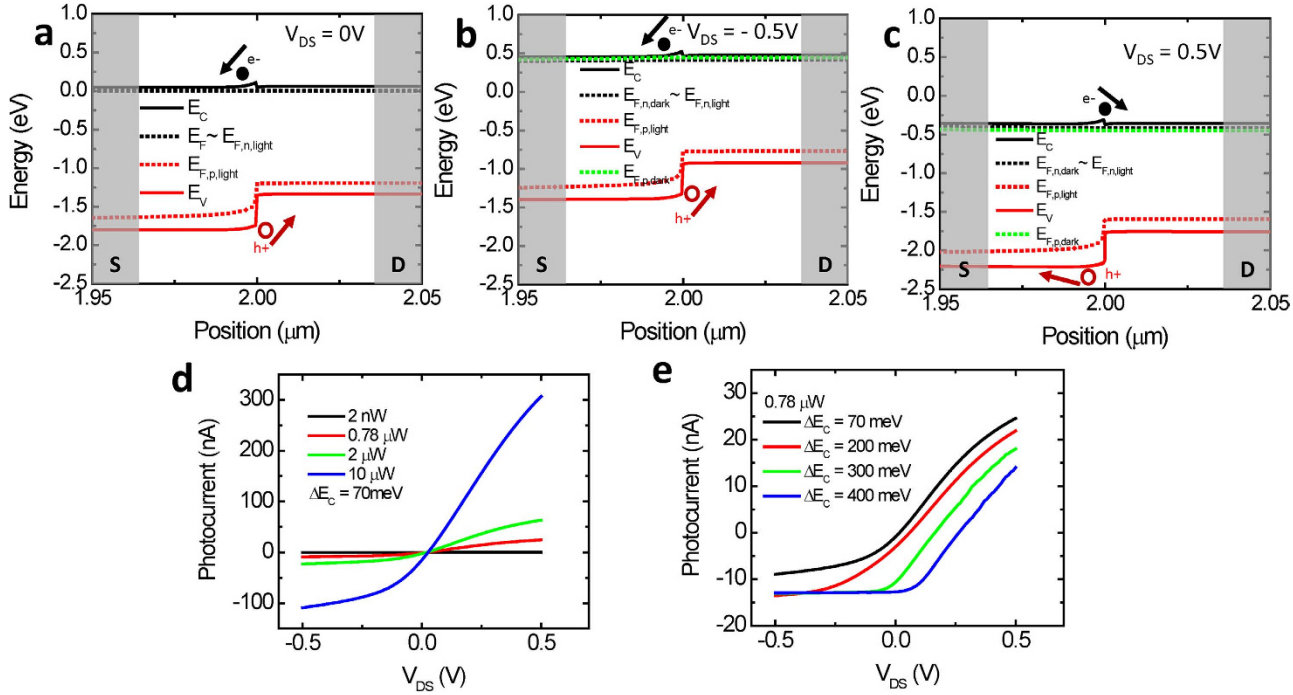

Figure 5. Simulated band diagrams at a, $V_{DS} = 0$ V, **b,** $V_{DS} = -0.5$ V and **c**, VDS = 0.5 V in dark and with light shined at the monolayer – multilayer MoS_2 junction. **d.** Simulated photocurrent vs. V_{DS} at different laser powers. **e.** Simulated photocurrent vs. V_{DS} with different ΔE_C values.

Photocurrent vs. applied V_{DS} is also simulated in TCAD Sentaurus with different illumination intensities. The same parameters and assumptions that are used to generate the band diagrams mentioned above are used to simulate the V_{DS} and the light intensity dependence of the photocurrent. In the SPCM measurements, as seen in Fig. 2c, at $V_{DS} = 0$ V a negative photocurrent is observed. As the applied bias is increased to $V_{DS} = 0.1$ V, photocurrent becomes positive (Fig. 2d). This implies that the experimental crossover from the negative photocurrent to positive photocurrent is in between $V_{DS} = 0$ V and $V_{DS} = 0.1$ V. The simulated photocurrents are shown in Fig. 5d–e. The simulation is in qualitative agreement with the experimental data, with the transition from the negative to positive photocurrent occurring at positive V_{DS} values. The negative to positive photocurrent crossover voltage is sensitive to the parameter values assumed for the simulations. Figure 5e illustrates the large dependence of the simulated crossover voltage on the ΔE_C value. Quantitative differences between the simulated and experimental data can also arise from the presence of a terraced junction as described in Fig. 1a, compared to the ideal step heterojunction simulated in Sentaurus. The Sentaurus simulations however qualitatively explain the experimental data and all the trends, but a quantitative analysis warrants simulations or first principle calculations using exact values of absorption coefficient, electron affinities, effective masses, doping, carrier lifetimes, diffusion lengths, etc.

In conclusion, the type-I heterojunctions enabled by lateral thickness modulation of MoS_2 are demonstrated. The junction properties are characterized by KPFM and SPCM. A workfunction difference of 80 meV is measured by KPFM. Furthermore, a conduction band offset of 70 meV is extracted from the difference in the electron affinities and work functions of the monolayer and multilayer regions of the MoS_2. Photocurrent generation at the monolayer-multilayer heterojunction is observed with SPCM. The peak photocurrent generation at the monolayer-multilayer junction is attributed to the electric field in the depletion region at the heterojunction formed by the difference in the work functions and the electron affinities of the monolayer and the multilayer flake. A short circuit current of 8 nA is measured due to the built-in electric field being able to separate and collect the generated electron hole pairs at the monolayer-multilayer junction. The photoresponsivity of the monolayer-multilayer MoS_2 junction is studied with respect to the incident light power and the source-drain bias. The demonstration of the type-I heterojunction on the same MoS_2 flake will inspire further investigation regarding the electronic transport properties of the atomically sharp type-I band alignment in the TMDC flakes.

Methods

The fabrication process for thickness modulated MoS_2 heterojunction devices is as follows. MoS_2 crystals (SPI Supplies) are transferred onto Si/SiO_2 (260 nm thick) substrates using the micromechanical exfoliation technique. The flakes of interest consisting of mono-multilayer junctions are identified using an

optical microscope. These flakes are formed naturally during the exfoliation process. In order to verify the thicknesses of the mono-multilayer regions, atomic force microscopy (AFM) is performed (Fig. 1a). Monolayer thickness of 0.7 nm is confirmed[1] and a multilayer thicknesses ranging from 6–15 nm is measured for the different samples explored in this study. Photoluminescence (PL) mapping of the flakes was conducted to further depict the mono- and multi-layer regions using a 532 nm pump laser with 8–80 μW power and a spot size of ~0.5 μm (Horiba Scientific LabRAM HR 800). PL map of a representative flake is shown in Fig. S1c, where the luminescence signal ratio is approximately one order of magnitude between the two regions of the MoS_2, further depicting the formation of a thickness modulated heterojunction. Metal source/drain (S/D) contacts are subsequently formed with one contact on the monolayer region and the other on the multilayer region of the MoS_2 flake. Electron-beam lithography was used to pattern the metal contacts, followed by evaporation of Ni/Au (30/30 nm), and lift-off of the resist in acetone.

References

1. Radisavljevic, B., Radenovic, A., Brivio, J., Giacometti, V. & Kis, A. Single-layer MoS_2 transistors. *Nat Nano*. **6,** 147–150 (2011).
2. Fang, H. *et al.* High-Performance Single Layered WSe_2 p-FETs with Chemically Doped Contacts. *Nano Lett*. **12,** 3788–3792 (2012).
3. Lopez-Sanchez, O., Lembke, D., Kayci, M., Radenovic, A. & Kis, A. Ultrasensitive photodetectors based on monolayer MoS_2. *Nat Nano*. **8,** 497–501 (2013).
4. Baugher, B. W. H., Churchill, H. O. H., Yang, Y. & Jarillo-Herrero, P. Optoelectronic devices based on electrically tunable p-n diodes in a monolayer dichalcogenide. *Nat Nano*. **9,** 262–267 (2014).
5. Ross, J. S. *et al.* Electrically tunable excitonic light-emitting diodes based on monolayer WSe_2 p-n junctions. *Nat Nano*. **9,** 268–272 (2014).
6. Cheng, R. *et al.* Electroluminescence and Photocurrent Generation from Atomically Sharp WSe_2/MoS_2 Heterojunction p–n Diodes. *Nano Lett*. **14,** 5590–5597 (2014).
7. Gong, Y. *et al.* Vertical and in-plane heterostructures from WS_2/MoS_2 monolayers. *Nat Mater*. **13,** 1135–1142 (2014).
8. Furchi, M. M., Pospischil, A., Libisch, F., Burgdörfer, J. & Mueller, T. Photovoltaic Effect in an Electrically Tunable van der Waals Heterojunction. *Nano Lett*. **14,** 4785–4791 (2014).
9. Fang, H. *et al.* A. Strong interlayer coupling in van der Waals heterostructures built from single-layer chalcogenides. *Proc. Natl. Acad. Sci. USA* **111,** 6198–6202 (2014).
10. Lee, C.-H. *et al.* Atomically thin p–n junctions with van der Waals heterointerfaces. *Nat Nano*. **9,** 676–681 (2014).
11. Kuc, A., Zibouche, N. & Heine, T. Influence of quantum confinement on the electronic structure of the transition metal sulfide. *Phys. Rev. B*. **83,** 245213 (2011).
12. Mak, K. F., Lee, C., Hone, J., Shan, J. & Heinz, T. F. Atomically Thin MoS_2: A New Direct-Gap Semiconductor. *Phys. Rev. Lett.* **105,** 136805 (2010).
13. Splendiani, A. *et al.* Emerging Photoluminescence in Monolayer MoS_2. *Nano Lett*. **10,** 1271–1275 (2010).
14. Howell, S.L. *et al.* Investigation of Band-Offsets at Monolayer–Multilayer MoS_2 Junctions by Scanning Photocurrent Microscopy. *Nano Lett.* **15,** 2278–2284 (2015).
15. Wu, C.-C. *et al.* Elucidating the Photoresponse of Ultrathin MoS_2 Field-Effect Transistors by Scanning Photocurrent Microscopy. *J. Phys. Chem. Lett*. **4,** 2508–2513 (2013).
16. Buscema, M. *et al.* Large and Tunable Photothermoelectric Effect in Single-Layer MoS_2. *Nano Lett*. **13,** 358–363 (2013).
17. Wang, X., Xie, W., Chen, J. & Xu, J.-B. Homo- and Hetero- p–n Junctions Formed on Graphene Steps. *ACS Appl. Mater. Interfaces*. **6,** 3–8 (2013).
18. Ko, C., Yang, Z. & Ramanathan, S. Work Function of Vanadium Dioxide Thin Films Across the Metal-Insulator Transition and the Role of Surface Nonstoichiometry. *ACS Appl. Mater. Interfaces*. **3,** 3396–3401 (2011).
19. Nonnenmacher, M., O'Boyle, M. P. & Wickramasinghe, H. K. Kelvin probe force microscopy. *Appl. Phys. Lett.* **58,** 2921–2923 (1991).
20. Melitz, W., Shen, J., Kummel, A. C. & Lee, S. Kelvin probe force microscopy and its application. *Surf. Sci. Rep.* **66,** 1–27 (2011).
21. Ochedowski, O. *et al.* Effect of contaminations and surface preparation on the work function of single layer MoS_2. *Beilstein J. Nanotechnol.* **5,** 291–297 (2014).
22. Choi, S., Shaolin, Z. & Yang, W. Layer-number-dependent work function of MoS_2 nanoflakes. *J. Korean Phys. Soc.* **64,** 1550–1555 (2014).
23. Zahid, F., Liu, L., Zhu, Y., Wang, J. & Guo, H. A generic tight-binding model for monolayer, bilayer and bulk MoS_2. *AIP Adv.* **3,** 052111 (2013).
24. Santos, E. J. G. & Kaxiras, E. Electrically Driven Tuning of the Dielectric Constant in MoS_2 Layers. *ACS Nano*. **7,** 10741–10746 (2013).
25. Miller, C. *et al.* Unusually long free carrier lifetime and metal-insulator band offset in vanadium dioxide. *Phys. Rev. B*. **85,** 085111 (2012).
26. Balasubramanian, K., Burghard, M., Kern, K., Scolari, M. & Mews, A. Photocurrent Imaging of Charge Transport Barriers in Carbon Nanotube Devices. *Nano Lett*. **5,** 507–510 (2005).
27. Gu, Y., Romankiewicz, J. P., David, J. K., Lensch, J. L. & Lauhon, L. J. Quantitative Measurement of the Electron and Hole Mobility−Lifetime Products in Semiconductor Nanowires. *Nano Lett*. **6,** 948–952 (2006).
28. Graham, R., Miller, C., Oh, E. & Yu, D. Electric Field Dependent Photocurrent Decay Length in Single Lead Sulfide Nanowire Field Effect Transistors. *Nano Lett*. **11,** 717–722 (2010).
29. Fu, D. *et al.* Electrothermal Dynamics of Semiconductor Nanowires under Local Carrier Modulation. *Nano Lett*. **11,** 3809–3815 (2011).
30. Yu, D. & Graham, R. Scanning Photocurrent Microscopy in Semiconductor Nanostructures. *Mod. Phys. Lett. B*. **27,** 1330018 (2013).
31. Yin, Z. *et al.* Single-Layer MoS_2 Phototransistors. *ACS Nano*. **6,** 74–80 (2011).
32. Esmaeili-Rad, M. R. & Salahuddin, S. High Performance Molybdenum Disulfide Amorphous Silicon Heterojunction Photodetector. *Sci. Rep.* **3,** 2345; DOI:10.1038/srep02345 (2013).
33. Sze, S. M. *Semiconductor devices, physics and technology*. [668–669] (Wiley, New Jersey, 2007).
34. Li, H.-M. *et al.* Metal-Semiconductor Barrier Modulation for High Photoresponse in Transition Metal Dichalcogenide Field Effect Transistors. *Sci. Rep.* **4,** 4041; DOI: 10.1038/srep04041 (2014).
35. Fang, H. *et al.* Degenerate n-Doping of Few-Layer Transition Metal Dichalcogenides by Potassium. *Nano Lett*. **13,** 1991–1995 (2013).

36. Kang, J., Liu, W., Sarkar, D., Jena, D. & Banerjee, K. Computational Study of Metal Contacts to Monolayer Transition-Metal Dichalcogenide Semiconductors. *Phys. Rev. X.* **4,** 031005 (2014).
37. Bernardi, M., Palummo, M. & Grossman, J. C. Extraordinary Sunlight Absorption and One Nanometer Thick Photovoltaics Using Two-Dimensional Monolayer Materials. *Nano Lett.* **13,** 3664–3670 (2013).
38. Das, S., Chen, H.-Y., Penumatcha, A. V. & Appenzeller, J. High Performance Multilayer MoS_2 Transistors with Scandium Contacts. *Nano Lett.* **13,** 100–105 (2012).
39. Kaushik, N. *et al.* Schottky barrier heights for Au and Pd contacts to MoS_2. *Appl. Phys. Lett.* **105,** 113505 (2014).
40. Amani, M. *et al.* Growth-substrate induced performance degradation in chemically synthesized monolayer MoS_2 field effect transistors. *Appl. Phys. Lett.* **104,** 203506 (2014).
41. Kang, J., Liu, W. & Banerjee, K. High-performance MoS_2 transistors with low-resistance molybdenum contacts. *Appl. Phys. Lett.* **104,** 093106 (2014).

Acknowledgements

This work was funded by the Director, Office of Science, Office of Basic Energy Sciences, Material Sciences and Engineering Division of the U.S. Department of Energy under Contract No. DE-AC02-05CH11231. The device fabrication and characterization was funded by the Center for Low Energy Systems Technology (LEAST), one of six centers supported by the STARnet phase of the Focus Center Research Program (FCRP), a Semiconductor Research Corporation program sponsored by MARCO and DARPA.

Author Contributions

M.T., D.F. and A.J. designed the experiments. M.T., D.F., J.S.K., D.H.L. and C.K. carried out the experiments, S.B.D. performed the TCAD Sentaurus simulations. M.T., D.F., S.B.D., C.K., M.N., S.T., J.W. and A.J. contributed to the data analysis. M.T., S.B.D. and A.J., wrote the paper while all authors provided feedback.

Additional Information

Supplementary information accompanies this paper at http://www.nature.com/srep

Competing financial interests: The authors declare no competing financial interests.

How to cite this article: Tosun, M. *et al.* MoS_2 Heterojunctions by Thickness Modulation. *Sci. Rep.* **5**, 10990; doi: 10.1038/srep10990 (2015).